ELSEVIER

Chemical Engineering Journal 74 (1999) 129–146

Chemical Engineering Journal

Rheology, dynamics, and structure of hydrocarbon blends: a molecular dynamics study of *n*-hexane/*n*-hexadecane mixtures

Loukas I. Kioupis, Edward J. Maginn*

Department of Chemical Engineering, University of Notre Dame, Notre Dame, IN 46556, USA

Received 27 August 1998; received in revised form 30 December 1998; accepted 31 December 1998

Abstract

Equilibrium molecular dynamics (EMD) and non-equilibrium molecular dynamics (NEMD) simulations are carried out on *n*-hexane/*n*-hexadecane binary mixtures. Using EMD, dynamic properties such as the viscosity, self-diffusivity, and rotational relaxation, as well as static structural properties are computed at different compositions. Upon mixing, a slowing down of the dynamics of the smaller species is observed, while the dynamics of the long species increases. The fluids exhibit non-ideal mixing due to a non-random distribution of the methylene units of the chain molecules. By examining the short range structure of the fluid, a local clustering of the smaller chains is observed. NEMD is used to simulate shear Couette flow and compute the shear viscosity of the fluid, particularly in the non-linear viscoelastic regime. Phenomena such as shear thinning, normal stress effects and molecular alignment are observed. Two shear thinning transitions are observed for the case of mixtures. It is shown that this is a result of the two species having differing relaxation times and varying tendencies to align with the shear flow. The longer chains shear thin first and align more readily than the shorter ones. The effect this has on the overall properties and shear-thinning spectrum, and its relation to the dynamics of each species, is examined. © 1999 Elsevier Science S.A. All rights reserved.

Keywords: Molecular dynamics; Rheology; Viscoelasticity; Lubricants; Alkanes; Mixture

1. Introduction

The study of the rheology, viscoelasticity and transport properties of alkanes and their mixtures is of considerable practical interest. Alkanes are the main constituent of lubricant base stocks, which are a complex mixture of mostly branched and cyclic saturated hydrocarbons with sizes of 16–40 carbon atoms [1]. Molecules in this size range are generally too small to be treated with theories for polymeric materials, but are too large for their properties to be adequately described with classic liquid theories. As a result, it is difficult to predict the dependence of the fluid properties on the composition and structure of the individual species. Such knowledge would be useful as a means for ‘‘designing’’ new or improved lubricants. Lacking this kind of predictive capability, lubricant ‘‘design’’ is currently more of an art than a science, and relies heavily upon the experience and insight of formulation chemists as well as on costly trial-and-error experimentation. Since the number of choices available to the lubricant formulator is staggering[1], a purely combinatorial approach toward improved formulations is inadequate.

To address this shortcoming, methods are needed that can relate the molecular-level details of lubricant molecules to the resulting macroscopic performance characteristics. This will enable predictive models to be developed and will provide guidance in the development of new compounds and blends. A number of tools have been developed recently with this capability, including the surface forces apparatus (SFA) [2–5], quartz crystal microbalance [6], and force microscopy techniques [7]. In addition, molecular simulation methods employing Monte-Carlo (MC) and molecular dynamics (MD) have been used as predictive tools to advance our understanding of friction and lubrication [8–43]. The literature in the general area of ‘‘molecular tribology’’ is extensive. Some of the issues examined include

---

*Corresponding author. Tel: +1-219-631-5687; fax: +1-219-631-8366; e-mail: ed@nd.edu

[1] For example, it has been estimated that a paraffinic molecule containing 25 carbon and 52 hydrogen atoms can have approximately 37,000,000 different molecular rearrangements. When one considers the naphthenic and aromatic species that also have 25 carbon atoms, it is clear that the number of choices, even when one is restricted to 25 carbon atoms, is immense.

1385-8947/99/$ – see front matter © 1999 Elsevier Science S.A. All rights reserved.
PII: S1385-8947(99)00053-4

rheology and dynamics of bulk fluids [23–43]; density and solvation force oscillations [44,45]; preferential adsorption of long chains [5,46,47] ordering of molecules at surfaces [22,48,49]; the tendency of confined species to take on solid–like character [50,51] and stick–slip behavior and its molecular origins [7,21]. These studies have helped elucidate many of the processes involved in lubrication and have laid a sound foundation upon which to build. However, there is still much work that needs to be done in this area before we can develop a set of "molecular design principles" upon which formulators can draw. For example, while the rheology and dynamics of pure fluids have been studied extensively by MD over the past decade, very little simulation work has been done on mixtures or the role additives play in determining lubricant properties. Early work on mixture behavior was confined mainly to simple molecules modeled as Lennard-Jones spheres [38–41]. Recently, the shear viscosity of mixtures of polar molecules such as methanol and water have been studied using MD [42]. There are few simulation studies involving mixtures of more complex molecules such as hydrocarbons. Recently, Khare et al. [33] performed NEMD simulations of a mixture of n-C_{36}/n-C_{16} as a first step in this direction, but did not examine in detail the viscoelastic properties of the blend. Some work on the dynamics of polymer blends with MD has been performed by Kopf et al. [43], using a bead and spring model of a blend of chains of equal lengths but different bead masses.

In this work, equilibrium molecular dynamics (EMD) and non-equilibrium molecular dynamics (NEMD) simulations are used to examine the properties of a binary hydrocarbon blend. A mixture of n-hexane and n-hexadecane was chosen as a simple model of a blend involving a short and long molecule. These molecules are small enough such that all static and dynamic properties can be computed without excessive computational cost. The molecules are large enough, however, to exhibit behavior typical of real lubricants. In addition, the molecules are different enough in size to have significantly different relaxation times as well as non-ideal mixing behavior. Details of the simulation methodology are given in the next section, followed by a discussion of the results and then a brief summary of the major conclusions. Additional algorithmic details are given in Appendix A.

2. Simulation methodology

2.1. Algorithms

The procedures whereby EMD and NEMD are used to compute static and dynamic properties of fluids have been treated extensively in several excellent references [52–54]. Here, we summarize some of the essential features of our simulations and demonstrate how important quantities are computed.

The EMD simulations were carried out in the canonical ensemble by applying a Nosé–Hoover thermostat [55] to the classical equations of motion. The equations used in this work are given in Appendix A. The force on each particle, $\mathbf{F}_i$, is given by:

$$\mathbf{F}_i = -\frac{\partial \mathscr{V}_i}{\partial \mathbf{r}_i}, \tag{1}$$

where $\mathscr{V}_i$ is the potential energy which describes the interactions between particle i and the rest of the particles in the system. The equations of motion are supplemented with periodic boundary conditions to remove surface effects [52].

The shear viscosity can be obtained from a Green–Kubo expression [52]:

$$\eta = \frac{V}{k_B T}\int_0^\infty \langle P_{xz}(0)P_{xz}(t)\rangle \, dt, \tag{2}$$

where η is the shear viscosity, V the volume, k_B the Boltzmann's constant, T temperature, P_{xz} the xz component of the pressure tensor $\mathbf{P}$, and t is the time. $\langle P_{xz}(0)Pxz(t)\rangle$ is the autocorrelation function of the xz component of the pressure tensor and the brackets $\langle \ldots \rangle$ denote ensemble averaging. The pressure tensor can be computed in two ways. The first is through the "atomic" virial theorem:

$$\mathbf{P}V = \sum_i \frac{\mathbf{p}_i\mathbf{p}_i}{m_i} + \sum_i \mathbf{r}_i\mathbf{F}_i, \tag{3}$$

where $\mathbf{r}_i$ and $\mathbf{p}_i$ are the position and momenta vectors of particle i, m_i the mass, and the summations are over all atoms. An alternative form is the "molecular" virial where the summations are over all molecules, $\mathbf{r}_i$ and $\mathbf{p}_i$ are the positions and momenta of the centers of mass of molecule i, and $\mathbf{F}_i$ the total force on molecule i. Both methods were used, but only molecular virial values are reported here. Pressures computed using the atomic virial tended to be systematically lower than the molecular pressure by about 0.4 MPa. A similar result was obtained by Mondello and Grest [23,37]. Viscosities computed using the two different virial formulations were identical within the statistical accuracy of the simulations.

To increase the accuracy in the calculation of the shear viscosity from the Green–Kubo relation, all different off-diagonal components of the pressure tensor can be used, since the system is isotropic at equilibrium and the xz, xy, yz components are equivalent. In addition, Daivis and Evans [28] have shown that the accuracy in the computation of shear viscosity from EMD can be further improved by using all six components of the stress tensor. The shear viscosity can then be calculated from the integral

$$\eta = \frac{V}{10 k_B T}\int_0^\infty \langle \mathbf{P}^{os}(0) : \mathbf{P}^{os}(t)\rangle \, dt, \tag{4}$$

where $\mathbf{P}^{\mathrm{os}}$ is the symmetrized traceless pressure tensor with components $P^{\mathrm{os}}_{\alpha\beta}$ given by:

$$P^{\mathrm{os}}_{\alpha\beta} = \frac{P_{\alpha\beta} + P_{\beta\alpha}}{2} - \delta_{\alpha\beta}\left(\frac{1}{3}\sum_{\gamma} P_{\gamma\gamma}\right). \tag{5}$$

The operator : denotes the double product between tensors [56]. Eq. (4) was used in all our EMD calculations.

In NEMD, an external field (perturbation) is introduced into the equations of motion and the response of the system at the non-equilibrium steady state is monitored [53]. Many NEMD algorithms have been proposed over the last 25 years [52,57] where usually a fictitious field is incorporated into the equations of motion. The method used in this work is the Sllod algorithm [53]. This algorithm has been used successfully by many authors [24–34,38–40,42,54] for computing viscosities of fluids. It has also been shown to be exact for arbitrarily large shear rates and is suitable for the study of the non-Newtonian behavior of fluids. The modified equations of motion for the Sllod algorithm are:

$$\frac{\mathrm{d}\mathbf{r}_i}{\mathrm{d}t} = \frac{\mathbf{p}_i}{m_i} + \mathbf{r}_i \cdot \nabla\mathbf{u}, \tag{6}$$

$$\frac{\mathrm{d}\mathbf{p}_i}{\mathrm{d}t} = \mathbf{F}_i - \mathbf{p}_i \cdot \nabla\mathbf{u}. \tag{7}$$

For planar Couette flow, $\mathbf{r}_i \cdot \nabla\mathbf{u} = (\dot{\gamma} r_{iz}, 0, 0)$ and $\mathbf{p}_i \cdot \nabla\mathbf{u} = (\dot{\gamma} p_{iz}, 0, 0)$, where z is the direction normal to the flow and x is the direction of flow. The shear rate is given by $\dot{\gamma} = \mathrm{d}u_x/\mathrm{d}z$. The momenta $\mathbf{p}_i$ are measured with respect to the streaming velocity and are called peculiar momenta. The Sllod algorithm is combined with the Lees–Edwards "sliding brick" periodic boundary conditions [58], where the periodic images above and below the central simulation box are moved in opposite directions. To use NEMD, several simulations are performed at varying shear rates, and the shear viscosity is found from the constitutive equation:

$$\eta(\dot{\gamma}) = \frac{-\langle P_{xz}\rangle}{\dot{\gamma}}. \tag{8}$$

The zero-shear Newtonian viscosity can be obtained from an extrapolation of the viscosity at $\dot{\gamma} \to 0$. The NEMD and EMD methods are formally equivalent, so that the extrapolated viscosity should agree with the equilibrium viscosity obtained from the Green–Kubo expression (Eq. (4)).

Application of the velocity field into the NEMD equations of motion causes the system to heat up. As with the EMD simulations, a Nosé–Hoover thermostat [55] was employed to maintain a constant temperature. This results in extra terms in the NEMD equations of motion, which are not shown in Eq. (5) and (6) for simplicity. The detailed equations used for constant temperature simulations are presented in Appendix A. We used the slightly modified equations of motion proposed by Martyna et al. [59], which can be shown to give the canonical distribution in an ergodic system.

One of the main problems with any MD technique is that long simulation times are typically required to examine complex molecule behavior. This problem is exacerbated by the large separation of timescales between relatively fast vibrational modes of bond lengths and angles and longer timescales that govern overall molecular motion. To reduce the severity of this problem, a multiple time step method has been employed for integrating the equations of motion. We used the rRESPA (reversible reference system propagator algorithm) method first proposed by Tuckerman et al. [60]. The method is based on a separation of the Liouville operator into the different modes that prescribe the motion of the atoms. With this separation, the fast vibrational forces are integrated with a small time step δt. The rest of the forces which prescribe the slow motion of the atoms are integrated with a larger time step $\Delta t = n\delta t$, where n is an integer. Consequently, the number of computationally expensive slow force evaluations are reduced for a given over all simulation time. Using this method, we were able to speed up the calculations by 5–10 times over a conventional algorithm. Details of the separation scheme used in this work are presented in Appendix B.

2.2. *Forcefield*

The n-alkanes were represented using a united atom (UA) model in which the hydrogen atoms are incorporated within the CH_3 and CH_2 groups. This results in a model with fewer interaction sites and substantial computational cost savings. The forcefield used in this work is a version of the TraPPE (Transferable Potentials for Phase Equilibria) model proposed by Siepmann et al. [61,62]. This forcefield has been optimized for phase behavior prediction and has been shown to reproduce accurately the liquid-vapor coexistence curve and predict the critical properties for several linear and branched alkanes. The potential model is an extension of the older Siepmann, Karaborni and Smit (SKS) model [63–65] for linear alkanes. The potential energy functions and the parameters used in this model are presented in Table 1. The potential energy model accounts for bond stretching, bond bending, torsional rotation and van der Waals non-bonded interactions. The non-bonded intermolecular interactions are modeled with a pairwise Lennard-Jones (LJ) potential. Intramolecular non-bonded interactions for sites separated by more than three bonds are also described by a LJ potential. For interactions between different groups a geometric combining rule is used, so that $\sigma_{ij} = (\sigma_{ii}\sigma_{jj})^{1/2}$ and $\epsilon_{ij} = (\epsilon_{ii}\epsilon_{jj})^{1/2}$. Bond-stretching and bond angle bending potentials are described with harmonic functions. A commonly used dihedral angle potential function proposed by Jorgensen et al. [66] was also used.

2.3. *Other simulation details*

EMD and NEMD simulations of the mixture were performed at six and four different compositions, respectively.

Table 1
Potential energy functions and parameters for the TraPPE united atom model used in this work

	Potential energy functions	Potential energy parameters
Non-bonded	$V_{LJ}=4\varepsilon_{ij}\,[(\sigma_{ij}/r_{ij})^{12}-(\sigma_{ij}/r_{ij})^{6}]$	$\sigma_{CH_3}=3.77$ Å $\varepsilon_{CH_3}/k_B=98.1$ K $\sigma_{CH_2}=3.93$ Å $\varepsilon_{CH_2}/k_B=47.0$ K
Bond stretching	$V_b=(1/2)k_b(r-r_0)^2$	k_b/k_B=452 900 K Å^{-2} r_0=1.54 Å
Bond-angle bending	$V_\theta=(1/2)k_\theta(\theta-\theta_0)^2$	k_θ/k_B=62 500 K/rad^2 θ_0=114°
Torsion	$V_\phi=a_0+a_1(1+\cos\phi)$ $+a_2(1-\cos 2\phi)$ $+a_3(1+\cos 3\phi)$	a_0/k_B=0.0 K a_1/k_B=355.03 K a_2/k_B=−68.19 K a_3/k_B=791.32 K

A small time step of $\delta t=1fs$ was used to integrate the fast modes and a large time step of $\Delta t=5fs$ was used for the slow modes. These time step sizes were chosen through a trial-and-error optimization procedure. Smaller time steps yielded essentially the same results. For the NEMD runs, the same size time steps were used for all different shear rates. No significant differences in the calculated properties were observed by using smaller time steps, even for the high shear rate runs.

The LJ potential was truncated at 9.825 Å, which is 2.5 times the σ value of the CH_2 groups. Long-range corrections were included in the calculation of the intermolecular energy and pressure. The values of the long-range corrections varied from −2.5 to −7.138 kJ/mol for the energy, and from −38.0 to −48.6 MPa for the pressure, depending on the composition of the mixture. Larger cutoff distances were also tested, but no appreciable differences in the results were observed. A neighbor list was also used to speed the calculations [52]. The EMD run lengths were varied from 2 to 23 ns, depending on the composition of the mixture. The NEMD runs varied from 150 ps to 5.6 ns depending on the shear rate and the system studied.

3. Results and discussion

3.1. Dynamic properties from EMD

The EMD simulations were performed in the canonical ensemble at experimental densities. Six different compositions of *n*-hexane and *n*-hexadecane were examined at ambient temperature. These conditions were chosen because they are relevant for lubrication applications and because experimental data were available at this state point. The simulated state points along with the calculated pressures are shown in Table 2. Viscosity, self-diffusivity and the rotational relaxation of the chains have been computed in order to study the dynamics of the alkane blend at different compositions. The calculated values are presented in Tables 3 and 4. Each of the properties studied is discussed in detail in the following subsections.

3.1.1. Shear viscosity

In Table 3, the shear viscosity values computed from EMD simulations are presented for the different systems studied. The values reported are the plateau values of the integral in Eq. (4) using the molecular virial with data collected every four large time steps (20 fs). The simulations were run for long times to minimize tail effects in the computation of the correlation functions. The error of the correlation function at long times t_{run} was estimated as [23,52]:

$$\sigma=\left(\frac{2\tau}{t_{run}}\right)^{1/2}, \tag{9}$$

where τ is the rotational relaxation time for the longer hydrocarbon in the mixture. Our runs were carried out for

Table 2
Simulated mixtures at different hexadecane mole fractions (x_{16})

x_{16}	ρ (g/cm^3)	N_{16}	N_6	P_{EMD} (MPa)
0.0	0.655	0	200	−3.9±0.8
0.2	0.698	40	160	−7.4±0.5
0.4	0.726	60	90	−11.0±0.5
0.6	0.745	60	40	−11.2±0.4
0.8	0.759	80	20	−13.7±0.5
1.0	0.770	100	0	−18.1±0.4

The densities reported are the experimental densities [67,68] at ambient conditions (298 K and 0.1 MPa) which have been used as an input for the simulations. N_{16} and N_6 stand for the number of hexadecane and hexane molecules used, respectively. P_{EMD} is the pressure calculated from EMD runs.

Table 3
Shear viscosity (η) results calculated from EMD simulations

x_{16}	η (mPa s)	t_{run} (ns)
0.0	0.204±0.017	2
0.2	0.401±0.053	10
0.4	0.466±0.064	12.5
0.6	0.663±0.091	16
0.8	0.999±0.136	20
1.0	1.129±0.159	23

The uncertainties in the simulated values have been obtained using Eq. (9) (see text).

Table 4
Self-diffusivity (D) and rotational relaxation times (τ) computed from EMD simulations

x_{16}	D (10^{-9} m^2/s)		τ (ps)	
	Hexadecane	Hexane	Hexadecane	Hexane
0.0	–	5.09±0.03	–	6.61±0.04
0.2	1.99±0.06	3.97±0.02	88.8±2.6	8.55±0.04
0.4	1.44±0.04	3.10±0.02	116.7±3.3	10.37±0.07
0.6	1.10±0.03	2.61±0.03	151.2±4.8	12.11±0.13
0.8	0.88±0.03	1.83±0.03	186.5±5.7	14.74±0.25
1.0	0.78±0.02	–	228.3±6.9	–
1.0[a]	0.576±0.008	–	300±15	–
0.0[b]	–	4.7	–	–
1.0[c]	0.379	–	–	–

The uncertainties in the simulations are $\simeq(2\tau/Nt_{\mathrm{run}})^{1/2}$ [52]. This is Eq. (9) with the extra factor $N^{1/2}$ in the denominator (N is the number of molecules for each species), because D and τ are single chain properties. The results have been computed from 5 ns runs, except for pure hexane where t_{run} is 2 ns.

[a] SKS value from simulations of pure n-hexadecane reported in [23].

[b] Experimental value for pure n-hexane. It has been obtained from an extrapolation using experimental self-diffusivity values of higher n-alkanes from the literature [69].

[c] Experimental value for pure n-hexadecane from [70].

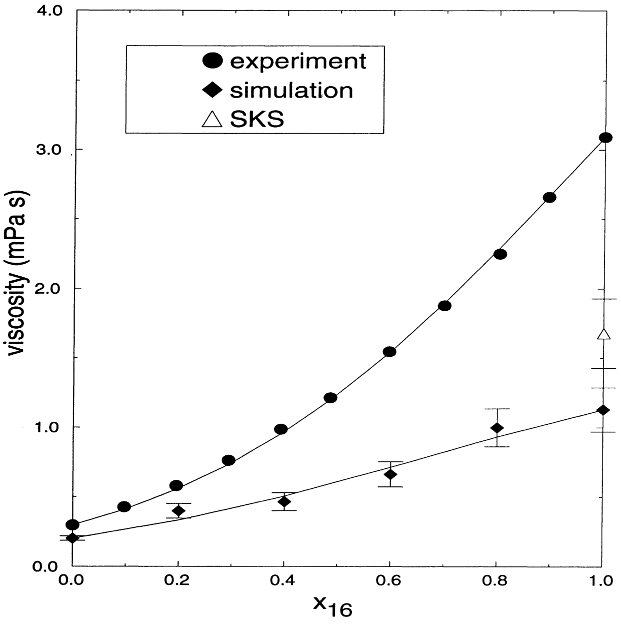

Fig. 1. Comparison of the EMD shear viscosity values with experimental values from [67], and the value from simulations using the SKS model from [23]. The solid lines are fits using Eq. (10).

times of approximately 100–120 times τ, which according to Eq. (9) yields a statistical uncertainty of about 15%. When carrying out the integral in Eq. (4), it is desirable to take the plateau value at the earliest possible time to minimize statistical error, and at later times to reduce systematic errors [23]. It was found that the Green–Kubo integral reached its plateau at about 1τ. The viscosity values reported are an average of the plateau values that were reached at times of between 1τ and 2τ.

In Fig. 1, shear viscosities computed from EMD simulations are plotted as a function of n-hexadecane mole fraction in the mixture. In the same plot, experimental values from the work of Aucejo et al. [67] are shown for comparison. It is clear that the TraPPE model under predicts the viscosity. The deviation of the simulated values from the experimental ones varies from 30% for pure n-C_6 to 60% for pure n-C_{16}, indicating that the forcefield does not perform as well for the longer alkanes. We note that the TraPPE model was optimized for linear alkanes up to n-C_{12} at conditions near the critical point. These conditions are very different from those of this study. In addition, at T=298 K n-C_{16} is only a few degrees above its melting point. Apparently, ambient conditions are a difficult state point for this particular forcefield. We also note that the TraPPE forcefield was developed for computing thermodynamic properties. The present results indicate that further work is needed in developing force fields that are able to predict both thermodynamic and transport properties over a range of conditions.

The computed viscosity for hexadecane using the SKS model [63–65] is also shown in Fig. 1. The SKS value is from simulations performed by Mondello and Grest [23]. The predicted value is slightly higher than the value computed using the TraPPE model, but still shows a large deviation from the experimental value.

Although the computed viscosities do not match exactly the experimental values, the simulations are still able to capture general trends. Moreover, important physical insight into the behavior of the mixture can be obtained from the simulations. As expected, the viscosity of the mixture increases with increasing concentration of the longer molecule. The solid lines in Fig. 1 fits according to the following semi-empirical [56]:

$$\ln\eta = x_1\ln\eta_1 + x_2\ln\eta_2 + 2x_1x_2G_{12}. \tag{10}$$

The adjustable interaction parameter G_{12} is 0.507 for the experiment and 0.469 for the simulations, indicating a positive deviation from ideal mixing for viscosity for both simulation and experiment. This is mainly due to the negative experimental excess molar volume of mixing [67,68] (i.e. higher density). Recall that the simulations were run in the canonical ensemble at experimental densities, for which there is a negative excess molar volume of mixing $\Delta\tilde{V}^{E}$. A negative $\Delta\tilde{V}^{E}$ means that there is a degree of compatibility between the two alkanes, which is due to the difference in the size of the two chains. The short chains are able to locate in the interstices between the longer chains, giving rise to a higher total density than would be predicted based on pure component properties. This negative excess volume of mixing gives rise to a positive deviation from ideal mixing for viscosity.

Ideally, one would study excess properties using simulations in the isothermal–isobaric (NPT) ensemble rather than the canonical (NVT) ensemble. We have in fact performed a number of NPT simulations, but prefer to examine viscosity by keeping density constant and allowing the pressure to fluctuate. The reason for this is that liquid properties are very strong functions of density but do not vary as strongly with pressure. This is especially true of the viscosity. As can be seen from Table 2, the force field does not adequately capture the pressure and density of the fluid simultaneously at the state point of interest, so we decided to fix the quantity that has the largest impact on the properties of interest (i.e. the density) at its experimental value.

3.1.2. Self-diffusivity

Computed self-diffusivities for each species in the binary mixture are shown in Table 4. These results were obtained by calculating the long time slope of the mean square displacement of the center of mass of each chain and applying the Einstein equation for diffusion [52]. The diffusion coefficients of both chains drop as the concentration of the longer chain increases. In the same table the experimental diffusion coefficients [69,70] for the pure compounds are shown, as well as the SKS value for the self-diffusivity of hexadecane from simulations done by Mondello and Grest [23] at the same conditions. Consistent with the viscosity calculations, the predicted values using the TraPPE model are somewhat higher than the experimental values. The TraPPE forcefield enables the chains to move more rapidly than they do in reality. However, the computed diffusivities are much closer to the experimental values than was the case for the viscosities.

3.1.3. Rotational diffusion

Another way to examine the dynamics of the chains, and how mixing affects each individual species in the blend, is to study rotational diffusion. The reorientational or rotational relaxation of the chain molecules is computed from the auto correlation function $\langle \mathbf{e}_1(0)\cdot\mathbf{e}_1(t)\rangle$ of the unit vector $\mathbf{e}_1$ of the longest axis of the molecules. For linear alkanes the longest axis can be assumed to be the end to end vector of the molecule. In Fig. 2 EMD results for the correlation functions are shown. The solid lines are from simulations of pure hexadecane and pure hexane. The dashed lines are the reorientational correlation functions for each species in a binary n-C$_6$/n-C$_{16}$ mixture with x_{16}=0.6. It is clear that upon mixing, the rotational dynamics of the long chains speed up, whereas the dynamics of the short chains slow down. The longer chains when dissolved in the matrix of short chains are able to move and rotate easier, resulting in faster relaxation rates. The short chains act as a plasticizer or solvent for the long chains. The exact opposite effect occurs for the short hexane chains; the presence of the large, slowly moving chains inhibits the rotational motion of the smaller chains. This behavior is observed for all different compositions simulated, as can be seen from Fig. 3, where the rotational relaxation times τ for each species in the mixture are plotted as a function of x_{16}. The relaxation times were computed by fitting the auto correlation functions to a series of exponentials:

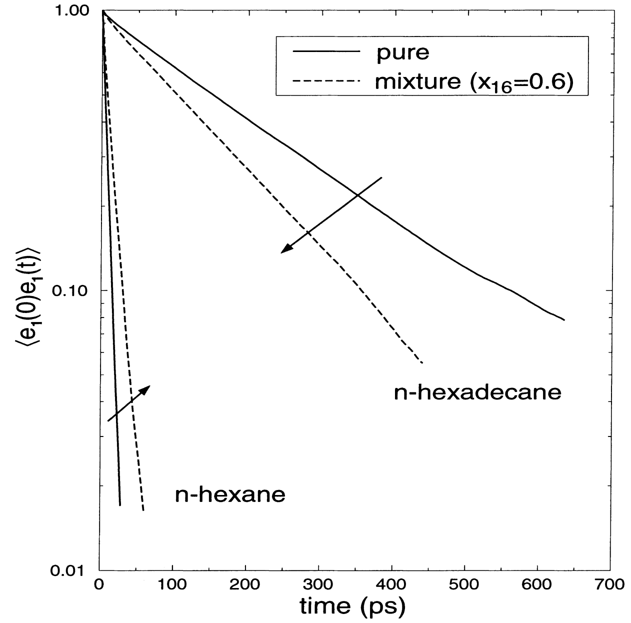

Fig. 2. End-to-end unit vector autocorrelation functions. The solid lines are the correlation functions for pure n-hexadecane and pure n-hexane, obtained from two different simulations. The dashed lines are the correlation functions for each species, obtained from a simulation of a mixture with x_{16}=0.6. The arrows indicate the change in the relaxation rate upon mixing.

$$\langle \mathbf{e}_1(0)\cdot\mathbf{e}_1(t)\rangle = \sum_i a_i \exp(-t/\tau_i). \qquad (11)$$

In our case only one exponential $\exp(-t/\tau)$ was enough to fit the correlation function curves, and the values of τ from

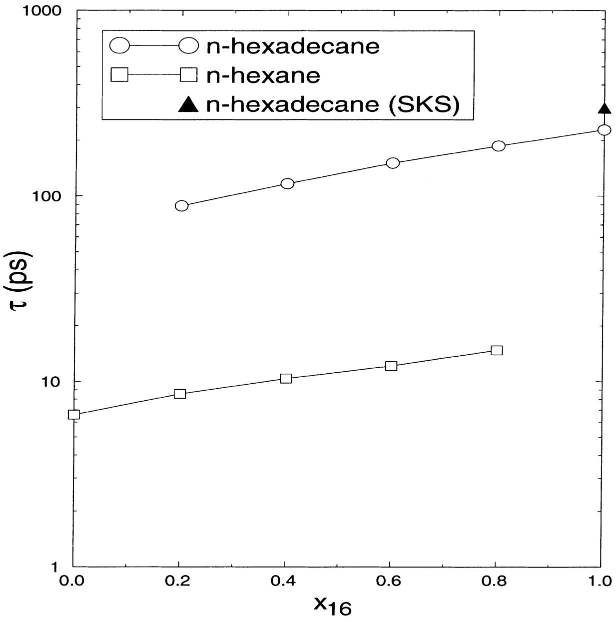

Fig. 3. Rotational relaxation times (τ) for each species in the mixture, as a function of the n-hexadecane mole fraction (x_{16}). The filled triangle shows the value of the relaxation time for pure n-hexadecane computed from simulations of [23] using the SKS potential model.

the fit are the ones reported in Table 4 and Fig. 3. The adequacy of a single exponential for fitting the relaxation spectra of short alkanes has also been reported by other groups [23,31,37]. We also tried fitting the spectra to the Kohlraush–Williams–Watt (KWW) equation [36]:

$$\langle \mathbf{e}_1(0) \cdot \mathbf{e}_1(t) \rangle = \exp[(-t/\tau)^{\beta}]. \tag{12}$$

The KWW equation accounts for the observation that the relaxation of complex systems follows a time-dependent rate. The β values from the fits were found to be always very close to unity (not shown), indicating that deviation from a single exponential mode is negligible. The values of τ reported in Table 4 were also compared with values of τ calculated from directly integrating the correlation functions. No significant differences were found between these two approaches. The rotational relaxation time obtained with the SKS model is shown as a filled triangle in Fig. 3. As was the case for the viscosity and self-diffusivity, the SKS forcefield exhibits slightly slower dynamics than the TraPPE model.

3.2. Static properties from EMD

3.2.1. Equilibrium fluid structure of pure components

The bulk properties of fluids are strongly influenced by local structure. To examine this, the inter-molecular pair correlation functions (PCF) $g(r)$ were computed to obtain insight into how the local molecular structure of the fluid impacts dynamic properties.

In Fig. 4 the PCF from EMD simulations of pure n-hexadecane and pure n-hexane are shown, for the different correlations between methyl–methyl, methyl–methylene and methylene–methylene groups. Insight into the local ordering of the different species can be gained by close examination of these curves. The initial CH_3–CH_3 peaks for both pure species are more intense than the other peaks, and they occur at shorter distances. The next highest peak is for the methyl–methylene groups, which is shifted to slightly larger distances. The smallest and most shifted peak is for methylene–methylene units. Fig. 4 shows that the ends of the chains are able to come closer to each other than the middle groups of the chains, which results in end groups contributing to better packing and more order. It is tempting to attribute this behavior to the fact that for the TraPPE forcefield, $\varepsilon_{CH_3} > \varepsilon_{CH_2}$ and $\sigma_{CH_3} < \sigma_{CH_2}$ (see Table 1). This implies that the methyl groups are relatively "small" and "attractive" compared to the methylene groups, and so exhibit more efficient packing. The fact that the model has a smaller Lennard-Jones size parameter for the CH_3 group than the CH_2 group is somewhat counter intuitive. However, this effect was also observed in simulations using the OPLS [66] forcefield and the SKS [63–65] forcefield in which $\sigma_{CH_3} = \sigma_{CH_2}$ [62]. We therefore conclude that the trends seen in Fig. 4 are mostly due to steric effects resulting from chain connectivity, and are not artifacts of the potential size parameters. For linear chains, it is easier for chain ends to come close together than for groups in the middle of the chain, where chain conformations are strongly governed by bond angles and torsion angles. The middle regions of the chains are effectively "screened" by the rest of the chain. It is easier for end groups to penetrate this steric barrier, which explains why the methyl–methylene peak is next highest.

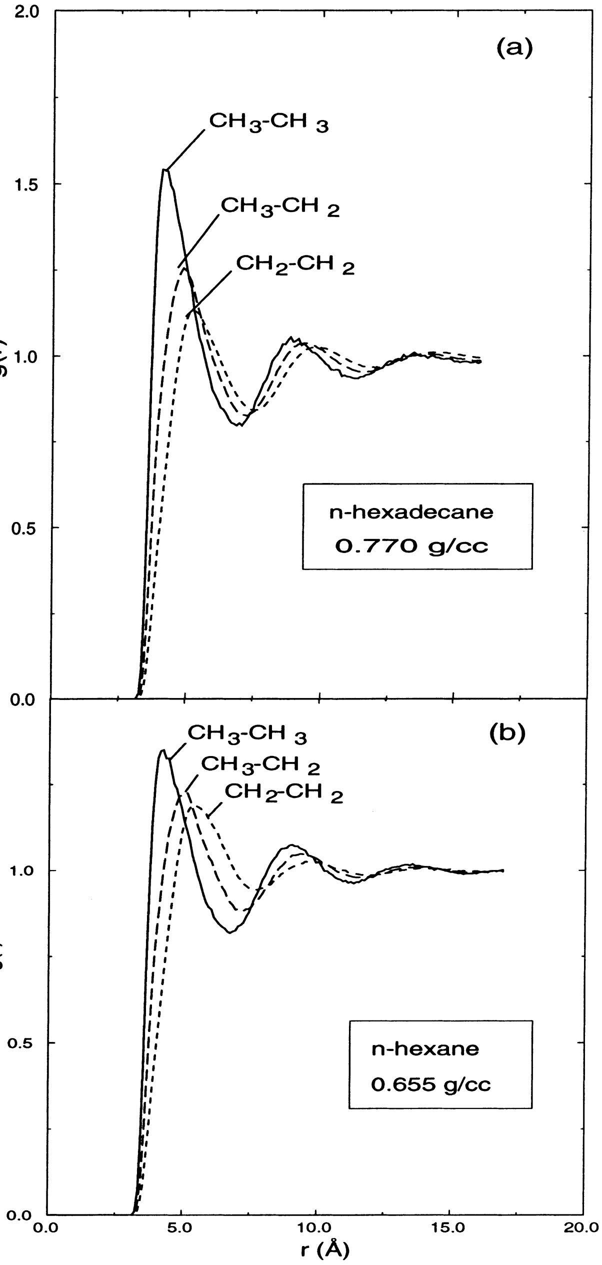

Fig. 4. Pair correlation functions between the different groups as a function of distance: (a) pure n-hexadecane; (b) pure n-hexane.

3.2.2. Local structure of the blend

In Fig. 5(a) the PCFs for the CH_2 groups of the different species in the blend are shown. This plot is for a blend at x_{16}=0.4, which is in the range of concentrations where the

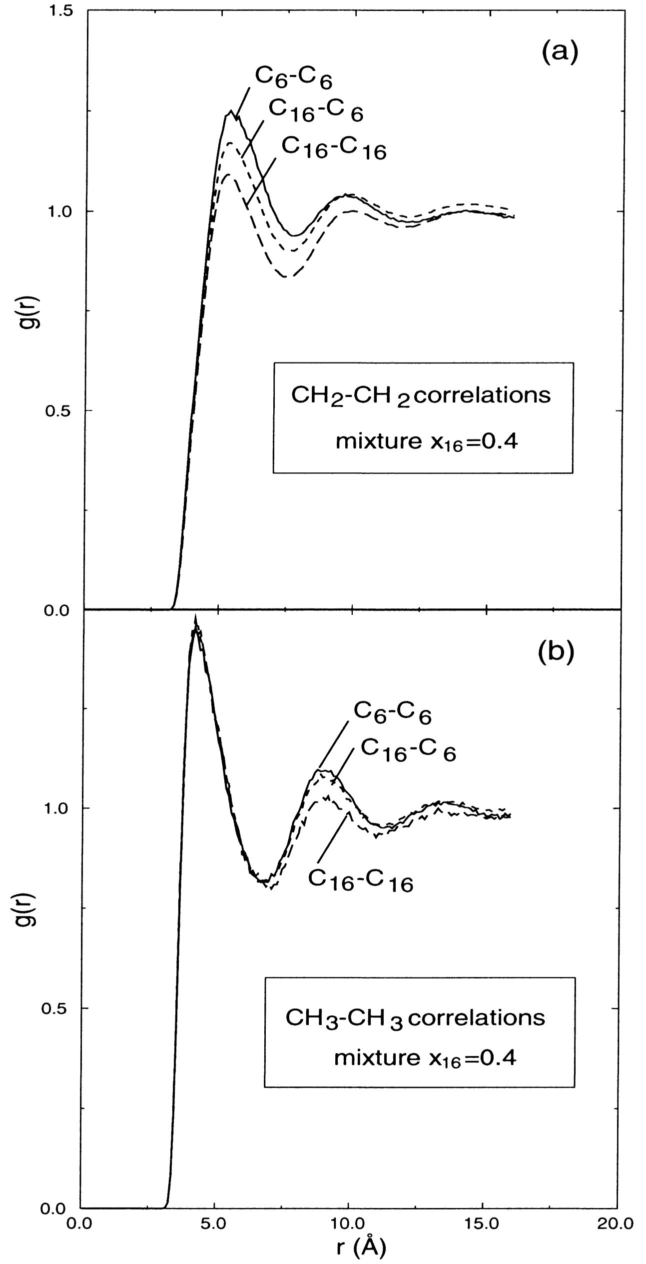

Fig. 5. Pair correlation functions between the inner and end groups for the different chains in a mixture of x_{16}=0.4: (a) CH_2–CH_2 pair correlations; (b) CH_3–CH_3 pair correlations.

maximum non-idealities are observed. It can be seen that there is non-random mixing between the inner sites of the different species. All three peak at almost the same separation distances. For all the compositions studied, however, the C_6–C_6 peak is higher. This means that there is a local clustering between the CH_2 groups of the short hexane chains in the mixture. On the other hand, the C_{16}–C_{16} PCF shows a lower peak than the C_{16}–C_6 curve, indicating a preferential C_{16}–C_6 structure. These results are mainly due to the difference in the sizes of the two chain molecules. The shorter hexane chains show a better packing and a stronger structure than the hexadecane chains. The hexane chains can be thought of as solvating the longer chains, while the bulkier C_{16} chains more effectively screen their inner groups.

On the other hand, a plot of the PCF for the CH_3 groups between the different species (Fig. 5(b)), shows random mixing in the first coordination shell, since all the curves coincide. Therefore, the end groups in linear alkane blends contribute to random mixing. This suggests that non-ideality will increase as chain length increases, due to the fact that the concentration of end groups will be lower for longer chains. This agrees with the experimental observation that non-ideality increases as the difference in size between species in a binary mixture increases [67,68]. Such an analysis raises the question as to what would happen in a mixture of branched hydrocarbons. Specifically, what is the impact of the degree of branching and the size and position of branches on the static and dynamic properties of a blend? It can be argued qualitatively that as the degree of branching increases (and thus the number of end groups) we can expect the mixture to behave more ideally. Conversely, as the length of the branches increases, then the relative fraction of end groups decreases and greater non-ideality should be observed. Simulations of the type described here may help provide answers to these kinds of questions. This issue is particularly relevant in lubrication, given that lubricant base stocks are comprised of a large percentage of branched hydrocarbons.

The local clustering of the short chains can also be seen from a plot of $g(r)$ between the center of mass of the different species in the blend (Fig. 6). Hexadecane clearly shows less structure than hexane, due to its increased flexibility and ability to take on more coiled-like conforma-

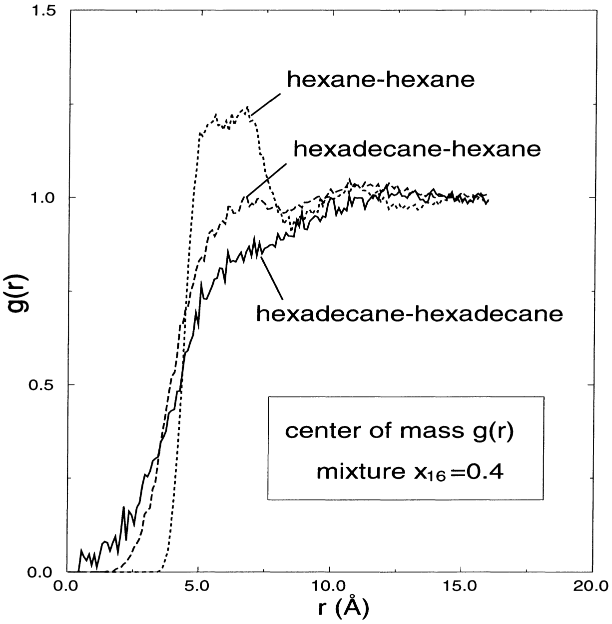

Fig. 6. Pair correlation functions for the center of mass of the chain molecules in a mixture of x_{16}=0.4.

tions. The hexane–hexane PCF has a high, broad peak at a separation of 4–8 Å, while no clear peak is observed for hexadecane. It would be interesting to use the PCFs to see how varying the composition impacts the ordering of the molecules. However, a direct comparison of the PCFs at different compositions can be misleading because the mixtures are at different bulk densities. A more suitable comparison can be obtained from a study of the local compositions, or the local mole fractions in the fluid [71]. To define this for our system, consider a binary mixture of molecules labeled as type *i* and type *j*. The number of nearest neighbors of component *i* surrounding another molecule of type *i* within a sphere of radius *L* is given by the coordination number:

$$N_{ii} = 4\pi\rho_i \int_0^L g_{ii} r^2 \, \mathrm{d}r. \tag{13}$$

Similarly, the coordination number of component *i* with respect to *j* molecules is:

$$N_{ji} = 4\pi\rho_j \int_0^L g_{ji} r^2 \, \mathrm{d}r. \tag{14}$$

Therefore, the local mole fraction of the *i* component around a reference central molecule of component *i* is given by:

$$x_{ii} = \frac{N_{ii}}{N_{ii}+N_{ji}} = \frac{4\pi\rho_i \int_0^L g_{ii} r^2 \, \mathrm{d}r}{4\pi\rho_i \int_0^L g_{ii} r^2 \, \mathrm{d}r + 4\pi\rho_j \int_0^L g_{ji} r^2 \, \mathrm{d}r} = \frac{x_i}{x_i + x_j G_{ji}}, \tag{15}$$

where

$$G_{ji} = \frac{4\pi \int_0^L g_{ji} r^2 \, \mathrm{d}r}{4\pi \int_0^L g_{ii} r^2 \, \mathrm{d}r},$$

and

$$x_{ii} + x_{ji} = 1.$$

Similar expressions can be written for the x_{jj} local mole fraction. The factor G_{ji} is a non-random factor indicating deviations from random mixing. If $G_{ji}=1$, then $x_{ii}=x_i$ (i.e. the mixing is random and there is no preferential clustering of the molecules). If $G_{ji}<1$, then $x_{ii}>x_i$, and there is a higher local clustering between molecules of type *i*. When $G_{ji}>1$, then $x_{ii}<x_i$, indicating a stronger local attraction between unlike molecules. The actual value of the x_{ii} depends on the choice of *L*, which is typically chosen to be the end of the first coordination shell (i.e. the first minimum in the PCF).

In Fig. 7(a) the local hexane composition x_{ii} for the different mixtures is plotted as a function of the distance from a central hexane molecule *i*. Similarly, in Fig. 7(b) the local hexadecane mole fraction x_{jj} is plotted as a function of a central hexadecane molecule *j*. At large distances, all curves approach the bulk mole fractions x_i and x_j. However, at the short distances between 5 and 8 Å where the first coordination shell was observed, the local mole fractions deviate from the bulk values indicating non-random mixing. For hexane in this region, x_{ii} is always higher than the bulk x_i value, indicating that there is a local clustering for the short chain molecules for all different mixtures studied. On the other hand, for hexadecane $x_{jj}<x_j$, indicating a stronger local preference between the unlike n-C_6 and n-C_{16} molecules.

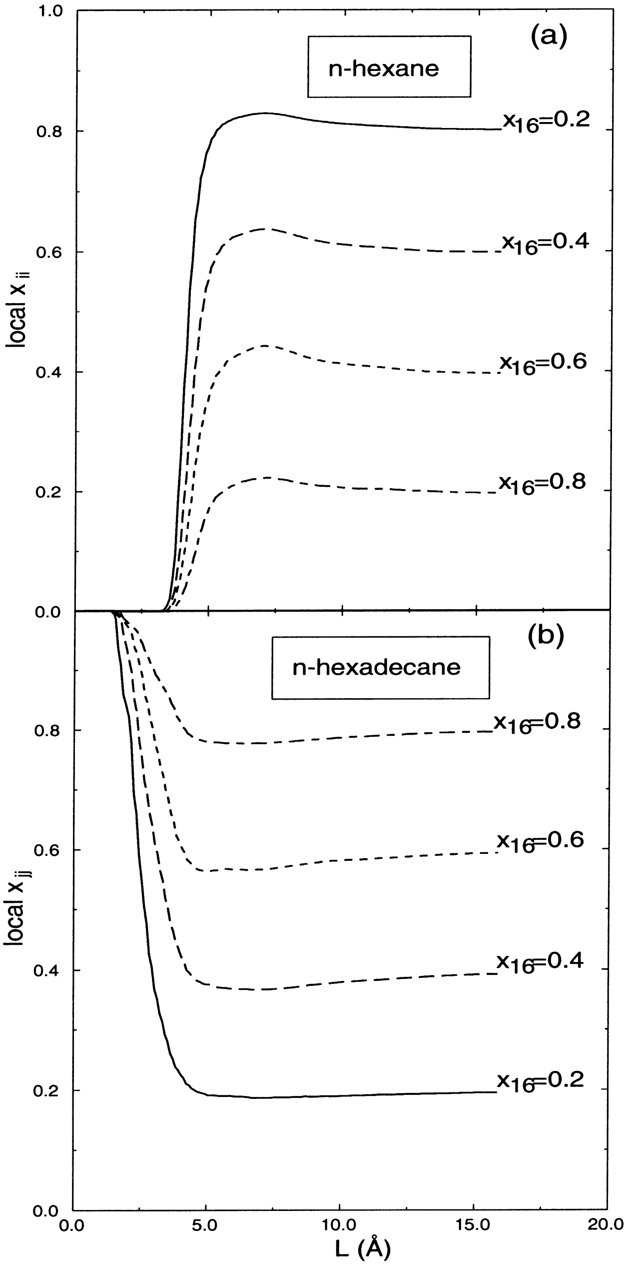

Fig. 7. Local mole fraction as a function of the distance *L* from a central molecule of the same type, at the different x_{16} bulk compositions studied; (a) *n*-hexane local compositions (x_{ii}); (b) *n*-hexadecane local compositions (x_{jj}).

At very short distances (below 4 Å), the local composition for hexane approaches zero ($x_{ii}\rightarrow 0$), while for hexadecane, $x_{jj} \rightarrow 1$. This does not indicate that both chains are surrounded by hexadecane molecules at very short distances. Rather, this behavior is an artifact caused by the slightly higher values of the PCF for the C_{16}–C_{16} center of mass correlations at very short distances, as shown in Fig. 6. The short hexane molecules can be thought of as having more hard core repulsion characteristics when compared to the floppier hexadecane chains. Therefore, at distances below 4 Å, no hexane molecules are present (see Fig. 6). On the other hand, the long hexadecane molecules are more flexible. Their centers of mass are more delocalized and exhibit less order. This causes the slightly higher concentrations of the centers of mass of C_{16} at very short distances, as shown from the center of mass PCF in Fig. 6. When integrating according to Eq. (15), the short-range local mole fraction x_{jj} for hexadecane jumps to 1 and x_{ii} for hexane is 0. This simply indicates that the center of mass is not a good measure of the location of the longer chains. Because of this, attention should only be paid to the regions of the first coordination shell and beyond when examining Fig. 7.

3.3. NEMD results

3.3.1. Shear viscosity

In Fig. 8 shear viscosity as a function of shear rate, computed using NEMD, is shown for pure hexadecane, pure hexane, and two different mixtures at x_{16}=0.6 and x_{16}=0.2. All results are listed in Table 5. It is clear that the fluid exhibits non-Newtonian behavior at high shear rates and at all different compositions, as the viscosity drops with increasing shear rate. This shear thinning behavior has been observed by many other groups from simulations of pure alkanes [24–34]. This same behavior is seen with polymeric materials, albeit at much lower shear rates. At low values of shear rate $\dot{\gamma}$, Newtonian behavior is recovered in which the viscosity is independent of shear rate. The plateau value at low shear rates determines the Newtonian viscosity and must agree with the value obtained from EMD simulations. The values of the Newtonian shear viscosity computed using the Green–Kubo expression from EMD simulations are also shown on the same plot for comparison. The agreement is good within the error of the simulations, especially for pure hexane and the more dilute x_{16}=0.2 blend. For pure hexadecane however, the Newtonian plateau value from NEMD is slightly higher than the EMD value. This indicates that longer times might be needed for the computation of viscosity from EMD for pure hexadecane. It is in general very difficult to find the viscosity from the integral of the stress–stress auto correlation function for long chain molecules. Due to long time tail effects in the correlation function, extremely long run times are needed. This makes NEMD simulations more effective and faster for the computation of shear viscosity of long alkanes, as compared with EMD. However, we should note that we continued the EMD run up to 33 ns and saw no significant change in the value of the viscosity when compared to a 23 ns run. Therefore, the discrepancy might be due to an underestimation of the NEMD error in the viscosity. The error in the NEMD values of the viscosity were estimated by breaking the total run into independent blocks of equal lengths. The error bars shown in Fig. 8 were estimated from the statistical variance of the average viscosity value over the blocks divided by the square root of the number of blocks. Therefore, in the calculation of the error of the total run we assume that the error is inversely proportional to the square root of the run length, which may underestimate the error of the total run. Another possible reason for this small discrepancy is the fact that the EMD values of the viscosity were computed using the molecular virial expression for the stress, whereas in NEMD the viscosity has been calculated from the atomic stress formalism. The molecular viscosity values from NEMD (not shown) were found to be always slightly lower than those computed with the atomic virial, and consequently in better agreement with the EMD values. Nevertheless, the differences are very small, and not larger than the statistical errors. The equivalence of the atomic and molecular stress expression in EMD simulations has been proven by several authors [23,30,31]. In NEMD the difference between the values of the stress tensor obtained from the molecular and atomic expressions is vanishingly small in the steady state limit for systems that are not subject to external torques [26]. In this paper, we prefer to report NEMD values of viscosity using the atomic stress expression, because the streaming velocity is applied to the atomic sites [26,31]. On the other hand, in the EMD calculation of the viscosity using the Green–Kubo equation, the molecular virial is preferred, because it exhibits less noise.

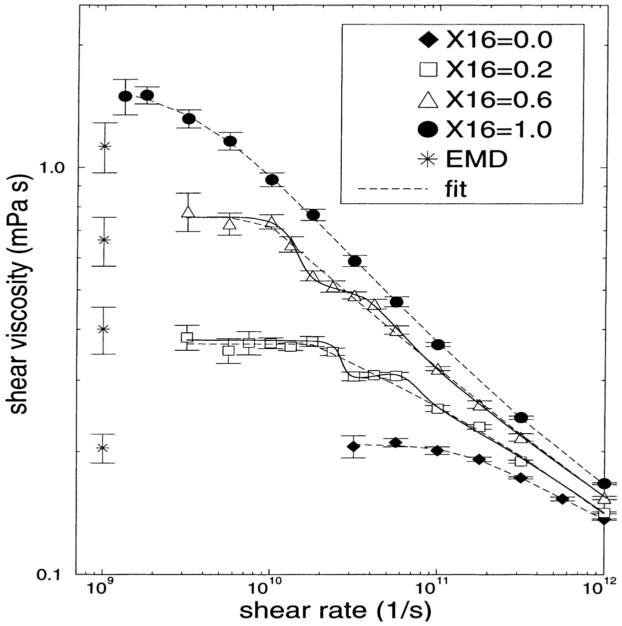

Fig. 8. Shear viscosity (η) versus shear rate ($\dot{\gamma}$) from NEMD simulations at four different compositions. The EMD viscosity values at the same compositions are also shown for comparison. The dashed lines are fits using Eq. (16). The solid lines have been drawn as a guide to the eye.

The dashed lines in Fig. 8 are fits to the simulated values using a generalized Cross/Carreau model [72]:

$$\eta = \eta_\infty + (\eta_0 - \eta_\infty)[1 + (\lambda\dot{\gamma})^\alpha]^{(n-1)/\alpha}. \tag{16}$$

Although the fit is good, it cannot capture exactly the shape of the curves for the mixtures. It is clear that the viscosity versus shear rate curves for the mixtures have two "bumps", as shown by the solid lines which have been drawn as a guide to the eye. We do not believe these bumps are artifacts of the simulations for two reasons. Firstly, the signal-to-noise ratio at these high shear rates is quite high, as indicated by the small error bars. Secondly, the shear rates that correspond to the bumps are approximately equal to the inverse of the rotational relaxation times of each species in the mixture calculated from the EMD simulations. It is well known that the critical shear rate $\dot{\gamma}^*$ where shear thinning starts to occur is related to the longest relaxation time of the fluid [24,25,31]. As discussed previously, the longest relaxation time for n-alkanes can be assumed to be the rotational relaxation time τ. For example, from the simulations of pure hexadecane, the logarithm of the critical shear rate where shear thinning occurs is $\log\dot{\gamma}^* = 9.6$, whereas from the EMD simulation of pure hexadecane the inverse of the rotational relaxation time (see Table 4) gives $\log(1/\tau_{16})$=9.64. In addition, for pure hexane we obtain $\log\dot{\gamma}^* = 11.12$ and $\log(1/\tau_6)$=11.18. For the x_{16}=0.6 mixture the first transition bump is observed at $\log\dot{\gamma}_1^* = 10.0$ and the second bump at $\log\dot{\gamma}_2^* = 10.6$. The logarithm of the inverse of the rotational relaxation time τ_{16} for hexadecane in the same mixture at equilibrium is $\log(1/\tau_{16})$=9.82 which is very close to the value of $\log\dot{\gamma}_1^* = 10.0$ of the first bump. Similarly, the rotational relaxation time in the same mixture for hexane as calculated from EMD gives $\log(1/\tau_6)$=10.9, which is very close to the $\log\dot{\gamma}_2^* = 10.6$ where the second bump occurred. The same applies for the x_{16}=0.2 blend. For this system $\log\dot{\gamma}_1^* = 10.32$ and $\log\dot{\gamma}_2^* = 10.75$ whereas $\log(1/\tau_{16})$=10.05 and $\log(1/\tau_6)$=11.06. Therefore, the two bumps showing two transitions to shear thinning correspond to two different mechanisms, each related to the different dynamics of each species.

It is known that shear thinning occurs due to increased alignment of the chains to the flow field, and this is directly related to the longest relaxation time τ. For shear rates higher than the inverse of the longest relaxation time of the system, the chain molecules do not have enough time to reorient and dissipate the energy due to shearing. Thus a rearrangement of the fluid molecules must take place and an increased intermolecular alignment occurs in order to relieve stress. When this occurs, the fluid has been moved into the non-linear viscoelastic regime (or non-Newtonian or pseudoplastic regime). The new structural configuration of the fluid results in lower viscosity, and the alignment caused by the applied shear results in a more ellipsoidal orientational distribution function of the fluid.

In the case of the blend two distinct critical shear rates are observed. The first corresponds to the start of shear-thinning and alignment of the longer chains described by the larger relaxation time. The short chains exhibit faster dynamics which are characterized by smaller relaxation times. They can be considered more mobile, therefore they can still respond fast enough to the external field. It can be assumed that they are still in the Newtonian or linear viscoelastic regime and able to dissipate energy due to viscous relaxation. Therefore, the main contribution of the first shear thinning region comes from the long hexadecane chains. In order for the shorter hexane chains to start contributing to the shear thinning, shear rates higher than the inverse of their relaxation time τ in the mixture are required. Thus, for $\dot{\gamma} > 1/\tau_6$ a second shear thinning transition occurs, and the short hexane chains start to align.

The fits shown in Fig. 8 cannot capture this spectrum. Another widely used model is the so-called Gleissle's rule [73], which relates the non-linear viscoelastic regime to the linear viscoelastic spectrum. In this approach, it is assumed that the non-linear behavior can be represented as a series of exponential terms resulting from applying the generalized Maxwell model of linear viscoelasticity to the non-linear viscoelastic regime:

$$\sigma_{ss} = \int_0^{t=1/\dot{\gamma}} G(t)\dot{\gamma}\,dt = \sum_i G_{0i}\lambda_i\dot{\gamma}[1 - \exp(-1/\dot{\gamma}\lambda_i)]. \tag{17}$$

This model, as well as a similar "Cox–Merz" rule [74], also failed to capture the two shear thinning transition "bumps" observed in Fig. 8. This is due to the fact that models of this type are empirical and used mainly for polymeric fluids. Polymers are long molecules with a broad spectrum of relaxation times and a high degree of polydispersity. In a polymer blend, these models predict a broadening of the relaxation spectrum and a broadening of the shear thinning transition region [72,75]. However, in the case of this clean binary mixture of the two relatively short n-alkanes with relaxation times that differ by an order of magnitude, two distinct transitions to shear thinning are observed. We believe this is the first time this has been observed in a simulation. It would be interesting to see if such behavior could be reproduced in the laboratory.

3.3.2. Normal stress effects

In Fig. 9 a plot of the first normal stress coefficient Ψ_1 versus $\dot{\gamma}$ is given. The first normal stress coefficient is defined as

$$\Psi_1 = \frac{P_{zz} - P_{xx}}{\dot{\gamma}^2}, \tag{18}$$

where Ψ_1 is a measure of the difference in the normal stresses observed in non-Newtonian fluids. An increase of the normal stresses suggests a tendency of the fluid to

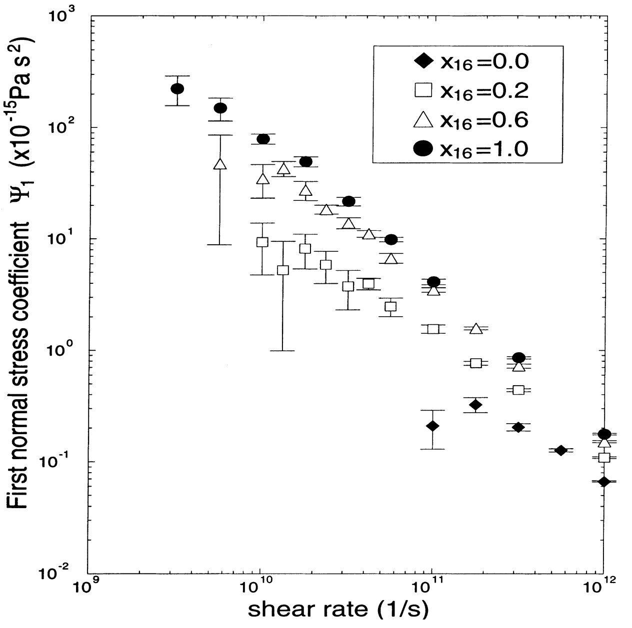

Fig. 9. First normal stress coefficients (Ψ_1) versus shear rate ($\dot{\gamma}$) computed from NEMD simulations at four different compositions. The error bars, σ_{Ψ_1} have been computed from the expression $\sigma_{\Psi_1} = \sqrt{(\sigma^2_{P_{zz}} + \sigma^2_{P_{xx}})/\dot{\gamma}^2}$ using the standard deviations of the P_{zz} and P_{xx} average values from the simulations.

deform in the normal directions (known as shear dilatancy) and in particular in the z-direction which is perpendicular to the shearing planes xy. Rheological studies of the non-linear viscoelasticity of polymers under simple Couette shear flow have shown that not far from the linear Newtonian regime P_{zz}–P_{xx} is proportional to $\dot{\gamma}_2$ [72] and thus Ψ_1 is constant. At higher shear rates Ψ_1 decreases. Exactly the same trend is observed in our simulations as shown in Fig. 9. These results are indicative of non-Newtonian behavior and suggest that the fluid is clearly in the non-linear viscoelastic regime. It is also clear that higher normal differences are obtained as x_{16} increases. Calculations such as these for various mixtures could help provide insight into ways of "tuning" the normal stress behavior of a particular fluid by changing the composition of the mixture.

3.3.3. Shear alignment and structural order

To further examine the shear thinning behavior, we investigated the structural order and degree of alignment of the fluid under shear. We have used the order tensor defined as [27,31]:

$$\mathbf{S} = \frac{3}{2}\left\langle \frac{1}{N}\sum_{i=1}^{N}\left(\mathbf{e}_{1i}\mathbf{e}_{1i} - \frac{1}{3}\mathbf{I}\right)\right\rangle, \tag{19}$$

where, $\mathbf{e}_{1i}$ is the unit vector along the end to end vector (longest axis) of the molecule i, and $\mathbf{I}$ is the unit tensor. The order tensor is a measure of the anisotropy of the average inertia tensor of a flexible molecule caused by the shear field. The largest eigenvalue λ of the order tensor is called the order parameter, and the eigenvector corresponding to the largest eigenvalue λ has the same direction as the longest semi-axis of an inertially equivalent ellipsoid to the fluid. The value of λ can vary from zero for randomly oriented (disordered) fluid at equilibrium, to unity for perfect orientational alignment.

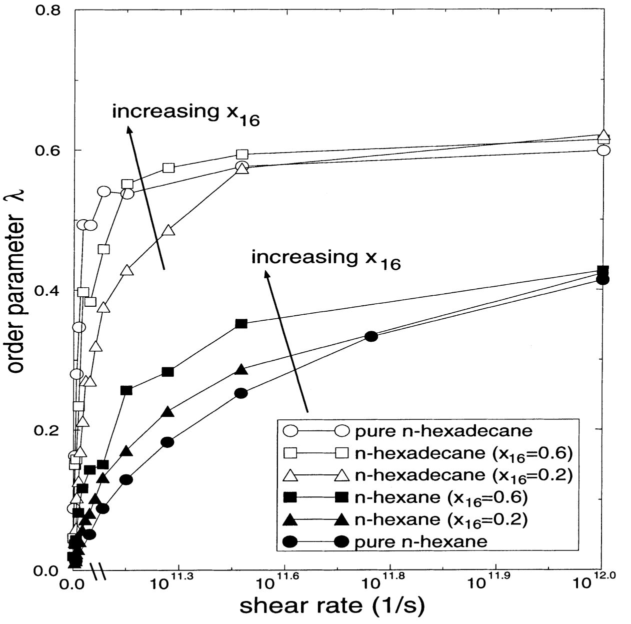

Fig. 10. Order parameter (λ) for each species versus shear rate ($\dot{\gamma}$), computed from NEMD simulations at four different mixture compositions.

In Fig. 10, λ is plotted as a function of the shear rate for each species in the mixtures, as well as for the pure components. The general trend is that λ increases with shear rate indicating an increased orientational ordering and more pronounced alignment of the chains at higher shear rates. In addition, it seems that the order parameter λ rises towards a plateau value, which might correspond to a saturation effect in the alignment and the beginning of a second Newtonian regime at very high shear rates. By examining the order parameter for each species in Fig. 10, it is seen that the hexadecane chains always have higher values of λ than the short hexane chains (i.e. they exhibit a higher degree of alignment). What's more interesting is that the order parameter of the longer C_{16} chains rises more rapidly (i.e. at lower shear rates) than that of the shorter C_6 chains. Finally, increasing the concentration of hexadecane, both the order parameter λ and the shear rate at which significant order takes place decrease. These results show that the two different species clearly exhibit different degrees of alignment with respect to the flow field. The longer chains start ordering at smaller shear rates, and the critical shear rate at which alignment occurs is also affected by the composition of the mixture. This supports the earlier conclusion as to the molecular origin of the "bumps" in Fig. 8.

To examine alignment further, an alignment angle can be defined as the angle between the principal eigenvector with

Table 5
Shear viscosity (η) values from NEMD simulations at different shear rates ($\dot{\gamma}$) and hexadecane mole fractions (x_{16})

$\log\dot{\gamma}$ (s^{-1})	x_{16}=0.0		x_{16}=0.2		x_{16}=0.6		x_{16}=1.0	
	η (mPa s)	t_{run}(ps)	η (mPa s)	t_{run} (ps)	η (mPa s)	t_{run} (ps)	η (mPa s)	t_{run} (ps)
9.12							1.497±0.150	5600
9.25							1.507±0.073	5000
9.50			0.382±0.027	3500	0.780±0.085	3000	1.318±0.067	3500
9.75			0.355±0.025	3000	0.728±0.046	2000	1.162±0.059	2200
9.87			0.371±0.024	2600				
10.00			0.370±0.011	2000	0.737±0.030	1200	0.934±0.036	1500
10.12			0.363±0.008	1600	0.647±0.028	750		
10.25			0.374±0.010	1200	0.542±0.016	600	0.766±0.024	900
10.37			0.353±0.007	900	0.510±0.016	600		
10.50	0.206±0.013	500	0.306±0.007	700	0.486±0.009	400	0.589±0.018	650
10.62			0.309±0.005	500	0.462±0.013	400		
10.75	0.211±0.005	350	0.307±0.006	400	0.399±0.009	400	0.468±0.013	400
11.00	0.201±0.004	250	0.255±0.004	300	0.320±0.004	300	0.367±0.004	300
11.25	0.192±0.002	200	0.230±0.003	300	0.261±0.006	300		
11.50	0.173±0.001	150	0.189±0.002	200	0.217±0.005	200	0.243±0.002	250
11.75	0.153±0.002	150						
12.00	0.137±0.001	150	0.142±0.001	200	0.154±0.001	200	0.167±0.001	250

The statistical uncertainties reported have been obtained from averages of different blocks of equal length.

the axis of the shearflow [27,31]. Values of the alignment (or "birefringence") angle are reported in (Table 5). Not surprisingly, these results show that the long chains align better with the flow. At high shear rates, the long chains align with an angle of about 9–10°, whereas the short chains with an angle of 20–24°. At low shear rates (Newtonian regime) the alignment angles reach the value of 45°, in agreement with the predictions of linear viscoelasticity theories [27,31].

3.4. Conclusions

We have studied the dynamic and structural properties of a binary mixture of *n*-hexadecane and *n*-hexane at different compositions. We have investigated the microscopic structure of the fluid under equilibrium conditions and under planar Couette flow, using both EMD and NEMD simulations and the TraPPE united atom forcefield. Dynamic properties such as the viscosity, self-diffusivity and rotational relaxation times were computed and found to be in fair to good agreement with experiment. In all cases, the dynamics of the molecules in the simulations were greater than those observed experimentally. Nevertheless, the simulations did capture the experimental trends in viscosity as a function of composition and are expected to provide an accurate qualitative picture of the binary fluid properties.

Table 6
Alignment angles for each species at different shear rates $\dot{\gamma}$ and different mixture compositions

$\log\dot{\gamma}$ (s^{-1})	x_{16}=0.0	x_{16}=0.2		x_{16}=0.6		x_{16}=1.0
	Hexane	Hexadecane	Hexane	Hexadecane	Hexane	Hexadecane
9.25						40.6°
9.50		46.8°	39.7°	40.5°	35.6°	30.4°
9.75		40.1°	39.1°	25.6°	34.6°	28.5°
9.87		41.5°	46.5°			
10.00		34.6°	38.5°	29.1°	34.9°	20.8°
10.12		32.0°	38.1°			
10.25		26.9°	38.0°	16.9°	27.7°	17.0°
10.37		24.5°	35.0°			
10.50	39.6°	27.3°	37.2°	16.9°	25.1°	14.6°
10.62		19.3°	33.3°			
10.75	41.0°	21.2°	35.5°	16.2°	26.5°	14.1°
11.00	40.0°	16.8°	30.5°	13.1°	24.9°	12.5°
11.25	34.3°	14.3°	29.9°	12.0°	23.0°	
11.50	30.3°	12.3°	27.0°	11.9°	22.3°	11.5°
11.75	26.2°					
12.00	23.8°	9.6°	22.0°	9.1°	20.3°	9.3°

Using the intermolecular pair correlation functions, the microscopic structure of the fluid at equilibrium was studied. It was observed that the system mixes non-ideally due to a non-random mixing of the CH_2 groups of the chains between the different species. A better packing and a preferential structure for the inner groups of the smaller chains was also observed, which results in a local clustering of the hexane molecules in the mixture.

NEMD simulations have also been used to compute the viscosity of the mixtures and study the non-linear viscoelastic behavior of the alkane blend under planar Couette flow. The system was shown to shear-thin and exhibit non-Newtonian behavior at high shear rates. However, each species in the mixture contributes differently to the shear-thinning, due to a different degree of alignment and orientational ordering of the chains to the flow. The longer chains align more readily and shear thin at smaller shear rates, giving rise to a non-linear viscoelastic spectrum that cannot be captured easily by any empirical models. Two "bumps" were observed in the shear-thinning spectrum, corresponding to two shear-thinning transitions at two distinct critical shear rates which are related to the rotational relaxation times of each species in the mixture.

Finally, it was observed that shorter simulation times are needed to compute the viscosity with NEMD than with EMD (Table 6). Combined with the fact that the NEMD simulations can be more easily parallelized by running simulations at different shear rates on different processors, we believe that NEMD is more efficient for the prediction of viscosity, especially for long chain molecules.

In the future we would like to extend this work to examine more complex molecules, such as branched hydrocarbons, longer chain alkane molecules and finally polymers, in an effort to understand the microscopic mechanisms of real lubricant and additive systems.

Acknowledgements

LIK thanks the State Scholarship Foundation of Greece for providing partial financial support for his graduate studies. The authors also acknowledge support from the Mobil Foundation, the National Science Foundation under grant CTS-9701470, and the U. S. Army Research Office under grant DAAG55-98-1-0091.

Appendix A

A.1 Equations of motion for NVT–Sllod dynamics

The Sllod equations of motion combined with the Nosé–Hoover thermostat for constant temperature simulations used in this work are [59,76]:

$$\dot{\mathbf{r}}_i = \mathbf{v}_i + \mathbf{i}\dot{\gamma} r_{zi}, \tag{A.1}$$

$$\dot{\mathbf{v}}_i = \frac{\mathbf{F}_i(\mathbf{r}_i)}{m_i} - v_\xi \mathbf{v}_i - \mathbf{i}\dot{\gamma} v_{zi}, \tag{A.2}$$

$$\dot{\xi} = v_\xi, \tag{A.3}$$

$$\dot{v}_\xi = G_\xi(v_i) = \frac{1}{Q}\left[\sum_i m_i v_i^2 - g k_B T\right], \tag{A.4}$$

where $\mathbf{r}_i$ and $\mathbf{v}_i$ are the position and peculiar velocity vectors of particle i, $\mathbf{F}_i$ the force on particle i, m_i the mass, $\dot{\gamma}$ the shear rate, ξ and v_ξ is the position and velocity of the thermostat and g the degrees of freedom of the system (g=3N). Q is the thermostat's mass and is given from $Q=\tau^2 g k_B T$ where τ is the Nosé thermostat time constant. Note that by setting $\dot{\gamma} = 0$, one can recover the EMD Nosé–Hoover equations of motion.

Appendix B

B.1 Time-reversible reference system propagator algorithm (rRESPA) for NVT–Sllod dynamics

Here, we present briefly the scheme used in this work for a multiple time step algorithm of the NVT–Sllod equations of motion. The methodology is based on the work of [60,76], and the final algorithm is very similar to the ones that have been proposed and used by other groups [29,30, 32]. The method is based on a separation of the Liouville operator iL into terms that prescribe different motion modes of the atoms in the system, such as fast modes due to vibrational forces in the molecule, or slow modes due to soft long range forces. These different modes are then integrated with different time steps. Here we present the decomposition of the total Liouville operator used in this work. The reader should refer to [60,76] for more details on the methods and the theory behind the formulation of time-reversible reference system propagator algorithms.

The Liouville operator for the NVT–Sllod equations of motion (see Appendix A is:

$$iL = \dot{\mathbf{r}} \cdot \frac{\partial}{\partial \mathbf{r}} + \dot{\mathbf{v}} \cdot \frac{\partial}{\partial \mathbf{v}} + \dot{\xi} \cdot \frac{\partial}{\partial \xi} + \dot{v}_\xi \cdot \frac{\partial}{\partial v_\xi}, \tag{B.1}$$

$$\begin{aligned} iL = {} & \mathbf{v} \cdot \frac{\partial}{\partial \mathbf{r}} + \dot{\gamma} r_z \cdot \frac{\partial}{\partial r_x} + \frac{\mathbf{F}}{m}\frac{\partial}{\partial \mathbf{v}} - v_\xi \mathbf{v} \cdot \frac{\partial}{\partial \mathbf{v}} - \dot{\gamma} v_z \cdot \frac{\partial}{\partial v_x} \\ & + v_\xi \cdot \frac{\partial}{\partial \xi} + G_\xi(\mathbf{v}) \cdot \frac{\partial}{\partial v_\xi}. \end{aligned} \tag{B.2}$$

We decompose the Liouville operator into the three propagators iL_1, iL_2 and iL_3:

$$iL_1 = \mathbf{v} \cdot \frac{\partial}{\partial \mathbf{r}} + \dot{\gamma} r_z \cdot \frac{\partial}{\partial r_x} + \frac{\mathbf{F}^{\mathrm{ref}}}{m} \cdot \frac{\partial}{\partial \mathbf{v}} - \dot{\gamma} v_z \cdot \frac{\partial}{\partial v_x}, \tag{B.3}$$

$$iL_2 = \frac{\mathbf{F} - \mathbf{F}^{\mathrm{ref}}}{m} \cdot \frac{\partial}{\partial \mathbf{v}}, \tag{B.4}$$

$$iL_3 = -v_\xi \mathbf{v} \cdot \frac{\partial}{\partial \mathbf{v}} + v_\xi \cdot \frac{\partial}{\partial \xi} + G_\xi(\mathbf{v}) \cdot \frac{\partial}{\partial v_\xi}. \tag{B.5}$$

The iL_1 operator is the reference operator and includes the shearing motion and the intramolecular bonded forces (bond-stretching, bond-angle bending and torsional rotation) into the $\mathbf{F}^{\mathrm{ref}}$ term (fast modes). The iL_2 operator includes the non-bonded LJ forces (intermolecular and intramolecular) which are considered as soft forces (slow modes). The iL_3 operator includes the thermostat terms. The reference operator that prescribes the fast motion modes can then be applied with a smaller time step, as shown below.

Using Trotter factorization, the evolution propagator can be written as:

$$\exp(iL\Delta t) = \exp\left(iL_3\frac{\Delta t}{2}\right)\exp\left(iL_2\frac{\Delta t}{2}\right)\exp(iL_1\Delta t) \times \exp\left(iL_2\frac{\Delta t}{2}\right)\exp\left(iL_3\frac{\Delta t}{2}\right), \tag{B.6}$$

$$\exp(iL\Delta t) = \exp\left(iL_3\frac{\Delta t}{2}\right)\exp\left(iL_2\frac{\Delta t}{2}\right)[\exp(iL_1\delta t)]^n \times \exp\left(iL_2\frac{\Delta t}{2}\right)\exp\left(iL_3\frac{\Delta t}{2}\right), \tag{B.7}$$

where the reference propagator $\exp(iL_1\delta t)$ is integrated with the smaller time step $\delta t=(\Delta t)/n$, n times. We further Trotter factorize the individual propagators $\exp(iL_1\delta t)$, $\exp(iL_2(\Delta t/2))$ and $\exp(iL_3(\Delta t/2))$ to get:

$$\begin{aligned}\exp(iL_1\delta t) = {} & \exp\left(\frac{\delta t}{2}\frac{\mathbf{F}^{\mathrm{ref}}}{m}\cdot\frac{\partial}{\partial \mathbf{v}}\right)\exp\left(-\frac{\delta t}{2}\dot{\gamma}v_z\cdot\frac{\partial}{\partial v_x}\right)\\ & \times\exp\left(\frac{\partial t}{2}\dot{\gamma}r_z\cdot\frac{\partial}{\partial r_x}\right)\exp\left(\delta t\mathbf{v}\cdot\frac{\partial}{\partial r}\right)\\ & \times\exp\left(\frac{\delta t}{2}\dot{\gamma}r_z\cdot\frac{\partial}{\partial r_x}\right)\exp\left(-\frac{\delta t}{2}\dot{\gamma}v_z\cdot\frac{\partial}{\partial v_x}\right)\\ & \times\exp\left(\frac{\delta t}{2}\frac{\mathbf{F}^{\mathrm{ref}}}{m}\cdot\frac{\partial}{\partial \mathbf{v}}\right),\end{aligned} \tag{B.8}$$

$$\exp\left(iL_2\frac{\Delta t}{2}\right) = \exp\left(\frac{\Delta t}{2}\frac{\mathbf{F}-\mathbf{F}^{\mathrm{ref}}}{m}\cdot\frac{\partial}{\partial \mathbf{v}}\right) \tag{B.9}$$

$$\begin{aligned}\exp\left(iL_3\frac{\Delta t}{2}\right) = {} & \exp\left(\frac{\Delta t}{4}G_\xi(\mathbf{v})\cdot\frac{\partial}{\partial v_\xi}\right)\exp\left(-\frac{\Delta t}{2}v_\xi\mathbf{v}\cdot\frac{\partial}{\partial \mathbf{v}}\right)\\ & \times\exp\left(\frac{\Delta t}{2}v_\xi\cdot\frac{\partial}{\partial \xi}\right)\times\exp\left(\frac{\Delta t}{4}G_\xi(\mathbf{v})\cdot\frac{\partial}{\partial v_\xi}\right).\end{aligned} \tag{B.10}$$

Substituting the above propagators into Eq. (B.7) we get the total propagator for the NVT–Sllod equations of motion.

The factorization scheme in Eq. (B.7) is called XO-RESPA (extended system outside-reference system propagator algorithm), because the Nosé–Hoover propagator $\exp(iL_3(\Delta t/2))$ is applied outside the reference system. If the motion prescribed by the $\exp(iL_3(\Delta t/2))$ occurs on the same timescale as the motion generated by the reference force, then a useful RESPA must include the application of this operator for the small time step δt [76]:

$$\begin{aligned}\exp(iL\Delta t) = {} & \exp\left(iL_3\frac{\delta t}{2}\right)\exp\left(iL_2\frac{\Delta t}{2}\right)\exp\left(-iL_3\frac{\delta t}{2}\right)\\ & \times\left[\exp\left(iL_3\frac{\delta t}{2}\right)\exp(iL_1\delta t)\exp\left(iL_3\frac{\delta t}{2}\right)\right]^n\\ & \times\exp\left(-iL_3\frac{\delta t}{2}\right)\exp\left(iL_2\frac{\Delta t}{2}\right)\exp\left(iL_3\frac{\delta t}{2}\right),\end{aligned} \tag{B.11}$$

or

$$\begin{aligned}\exp(iL\Delta t) = {} & \exp\left(iL_3\frac{\delta t}{2}\right)\exp\left(iL_2\frac{\Delta t}{2}\right)\exp(iL_1\delta t)\left(iL_3\frac{\delta t}{2}\right)\\ & \times\left[\exp\left(iL_3\frac{\delta t}{2}\right)\exp(iL_1\delta t)\exp\left(iL_3\frac{\delta t}{2}\right)\right]^{n-2}\\ & \times\exp\left(iL_3\frac{\delta t}{2}\right)\exp(iL_1\delta t)\exp\left(iL_2\frac{\Delta t}{2}\right)\\ & \times\exp\left(iL_3\frac{\delta t}{2}\right).\end{aligned} \tag{B.12}$$

The resulting integrator is named XI-RESPA (extended system inside-reference propagator algorithm), and is constructed so that when $n=1$ the original extended system algorithm Eq. (B.6) is recovered. In this work, all the results reported are from runs using the XI-RESPA version of the algorithm. The final solution (expressed in positions and momenta) is generated by applying serially the above evolution propagators to the initial state $\mathbf{\Gamma}(0)=\{\mathbf{r}(0),\mathbf{p}(0)\}$, in the same way, as shown in [60,76]. The application of the total evolution propagator is translated very easily into a program code.

Nomenclature

a_0, a_1, a_2, a_3	torsional potential energy function parameters (J)
D	self-diffusion coefficient (m^2/s)
$\mathbf{e}_1$	unit vector of the longest axis of the molecule
$\mathbf{F}_i$	force vector on particle i (N)
$\mathbf{F}^{\mathrm{ref}}$	forces that act on the reference system (N)
g	system's degrees of freedom
$g(r)$	pair correlation function
G_0	plateau modulus (MPa)
G_{12}	non-ideal mixing empirical parameter in Eq. (10)
G_{ji}	non-random factor
$G(t)$	shear modulus (MPa)
$\mathbf{I}$	unit tensor
k_{b}	bond stretching force constant (J/Å^2)
k_{B}	Boltzmann constant (J/K)
k_θ	bond-angle bending force constant (J/rad^2)
L	coordination shell size (Å)
m_i	mass of particle i (kg)

n	exponent in the generalized Cross/Carreau equation
n	number of small time steps
N	number of molecules
N_{ji}	number of molecules of component j around a molecule of component i
$\mathbf{p}_i$	momentum vector of particle i (kg m/s)
P	pressure (MPa)
$\mathbf{P}$	pressure (or stress) tensor (MPa)
$P_{\alpha\beta}$	component of pressure tensor, where α, β range over x, y, z (MPa)
$\mathbf{P}^{\mathrm{os}}$	symmetrized traceless pressure tensor (MPa)
Q	thermostat's mass (J/s^2)
r	separation distance (Å)
r, r_0	bond length and equilibrium bond length (Å)
$\mathbf{r}_i$	position vector of particle i (Å)
R	gas constant (kJ mol^{-1} K^{-1})
$\mathbf{S}$	order tensor
t_{run}	simulation time length (ns)
T	temperature (K)
$\mathbf{v}_i$	velocity vector of particle i (m/s)
v_ξ	thermostat's velocity (s^{-1})
V	volume of the simulation box (Å^3)
V_b	bond stretching potential energy (J)
V_{LJ}	non-bonded (Lennard-Jones) potential energy (J)
V_θ	bond-angle bending potential energy (J)
V_ϕ	torsional potential energy (J)
x, y, z	Cartesian coordinates
x_i	mole fraction of component i
x_{ji}	local mole fraction of component j around component i

Greek letters

α	exponent in the generalized Cross/Carreau equation
β	Kohlraush–Williams–Watt equation parameter
$\dot{\gamma}$	shear rate (s^{-1})
$\dot{\gamma}^*$	critical shear rate marking transition to shear-thinning behavior (s^{-1})
$\mathbf{\Gamma}(t)$	$\{\mathbf{r}(t), \mathbf{p}(t)\}$, phase space (6N dimensional set of positions and momenta)
δt, Δt	small and large time step (fs)
$\Delta\tilde{V}^E$	excess molar volume of mixing (cm^3/mol)
ε	Lennard-Jones energy parameter (J)
η	shear viscosity (mPa s)
η_0, η_∞	asymptotic viscosity at low and high shear rates respectively (mPa s)
θ, θ_0	bond angle and equilibrium bond angle (rad)
λ	order parameter
λ	parameter in the generalized Cross/Carreau equation (s)
λ_i	viscoelastic relaxation time (s)
ξ	thermostat's position
ρ	density (g/cm^3)
σ	Lennard-Jones size parameter (Å)
σ	statistical standard deviation
τ	Nosé thermostat time constant (s)
τ	rotational or reorientational relaxation time (s)
ϕ	torsion angle (rad)
Ψ_1	first normal stress coefficient (Pa s^2)

Special symbols

$\nabla\mathbf{u}$	velocity gradient (s^{-1})
iL	Louiville operator

References

[1] G.W. Stachowiak, A.W. Batchelor, Engineering Tribology, Elsevier, Amsterdam, 1993.

[2] J.N. Israelachvili, Intermolecular and Surface Forces, 2nd ed., Academic Press, London, 1992.

[3] H. Yoshizawa, J.N. Israelachvili, Fundamental mechanisms of interfacial friction. 2. Stick-slip friction of spherical and chain molecules, J. Phys. Chem. 97 (1993) 11300–11313.

[4] J. Van Alsten, S. Granick, Shear rheology in a confined geometry – polysiloxane melts, Macromolecules 23 (1990) 4856–4862.

[5] S. Granick, Motions and relaxations of confined liquids, Science 253 (1991) 1374–1379.

[6] E. Watts, J. Krim, A. Widom, Experimental observation of interfacial slippage at the boundary of molecularly thin films with gold substrates, Phys. Rev. B 41 (1990) 3466–3472.

[7] B. Bhushan (Ed), Handbook of Micro/Nanotribology, CRC Press, Boca Raton, 1995.

[8] J. Magda, M. Tirrell, H.T. Davis, Molecular dynamics of narrow, liquid-filled pores, J. Chem. Phys. 83 (1985) 1888–1901.

[9] M. Schoen, J.H. Cushman, D. Diestler, C.L. Ryhkerd, Fluids in micropores. II. Self-diffusion in a simple classical fluid in a slit pore, J. Chem. Phys. 88 (1988) 1394–1406.

[10] P.A. Thompson, M.O. Robbins, Shear flow near solids: epitaxial order and flow boundary conditions, Phys. Rev. A 41 (1990) 6830–6837.

[11] Y. Wang, K. Hill, J.G. Harris, Comparison of branched and linear octanes in the surface force apparatus. A molecular dynamics study, Langmuir 9 (1993) 1983–1985.

[12] Y. Wang, K. Hill, J.G. Harris, Confined thin films of a linear and branched octane. A comparison of the structure and solvation forces using molecular dynamics simulations, J. Chem. Phys. 100 (1994) 3276–3285.

[13] P. Padilla, Chemical structure effects on the equilibrium and under shear properties of thin films in confined geometries: A molecular dynamics simulation study, J. Chem. Phys. 103 (1995) 2157–2168.

[14] M. Vacatello, D.Y. Yoon, B.C. Laskowski, Molecular arrangements and conformations of liquid *n*-tridecane chains confined between two hard walls, J. Chem. Phys. 93 (1990) 779–786.

[15] I. Bitsanis, G. Hadziioannou, Molecular dynamics simulations of the structure and dynamics of confined polymer melts, J. Chem. Phys. 92 (1990) 3827–3847.

[16] M. Lupkowski, F. van Swol, Ultrathin films undershear, J. Chem. Phys. 95 (1991) 1995–1998.

[17] S.Y. Liem, D. Brown, J.H.R. Clarke, Investigation of the homogeneous-shear nonequilibrium-molecular-dynamics method, Phys. Rev. A 45 (1992) 3706–3713.

[18] P. Padilla, S. Toxvaerd, Simulating shear flow, J. Chem. Phys. 104 (1996) 5956–5963.

[19] P. Padilla, S. Toxvaerd, Fluid alkanes in confined geometries, J. Chem. Phys. 101 (1994) 1490–1502.

[20] J. Gao, W.D. Luedtke, U. Landman, Nano-elasto hydrodynamics: structure, dynamics, and flow in nonuniform lubricated junctions, Science 270 (1995) 605–608.

[21] B. Bhushan, J.N. Israelachvili, U. Landman, Nanotribology: friction, wear, and lubrication at the atomic scale, Nature 374 (1995) 607–616.

[22] W.J. Ma, L.K. Iyer, S. Vishveshwara, J. Koplik, J.R. Banavar, Molecular-dynamics studies of systems of confined dumbbell molecules, Phys. Rev. E 51 (1995) 441–453.

[23] M. Mondello, G.S. Grest, Viscosity calculations of *n*-alkanes by equilibrium molecular dynamics, J. Chem. Phys. 106 (1997) 9327–9336.

[24] A. Berker, S. Chynoweth, U.C. Klomp, Y. Michopoulos, Non-equilibrium molecular dynamics (NEMD) simulations and the rheological properties of liquid *n*-hexadecane, J. Chem. Soc., Faraday Trans. 88 (1992) 1719–1725.

[25] S. Chynoweth, R.C. Coy, Y. Michopoulos, Simulated non-Newtonian lubricant behavior under extreme conditions, J. Engr. Tribology 209 (1995) 243–254.

[26] R. Edberg, G.P. Morris, D.J. Evans, Rheology of *n*-alkanes by nonequilibrium molecular dynamics, J. Chem. Phys. 86 (1987) 4555–4570.

[27] P.J. Daivis, D.J. Evans, G.P. Morris, Computer simulation study of the comparative rheology of branched and linear alkanes, J. Chem. Phys. 97 (1992) 616–627.

[28] P.J. Daivis, D.J. Evans, Comparison of constant pressure and constant volume non-equilibrium simulations of sheared model decane, J. Chem. Phys. 100 (1994) 541–547.

[29] C.J. Mundy, J.I. Siepmann, M.L. Klein, Decane under shear: A molecular dynamics study using reversible NVT–SLLOD and NPT–SLLOD algorithms, J. Chem. Phys. 103 (1995) 10192–10200.

[30] S.T. Cui, P.T. Cummings, H.D. Cochran, Multiple time step non-equilibrium molecular dynamics simulation of the rheological properties of liquid *n*-decane, J. Chem. Phys. 104 (1996) 255–262.

[31] S.T. Cui, S.A. Gupta, P.T. Cummings, H.D. Cochran, Molecular dynamics simulations of the rheology of normal decane, hexadecane, and tetracosane, J. Chem. Phys. 105 (1996) 1214–1220.

[32] Z. Xu, J. de Pablo, S. Kim, Transport properties of polymer melts from non-equilibrium molecular dynamics, J. Chem. Phys. 102 (1995) 5836–5844.

[33] R. Khare, J. de Pablo, A. Yethiraj, Rheological, thermodynamic, and structural studies of linear and branched alkanes undershear, J. Chem. Phys. 107 (1997) 6956–6964.

[34] M. Lahtela, M. Linnolahti, T.A. Pakkanen, R.L. Rowley, Computer simulations of branched alkanes: the effect of side chain and its position on rheological behavior, J. Chem. Phys. 108 (1998) 2626–2630.

[35] P. Padilla, S. Toxvaerd, Self-diffusion in *n*-alkane fluid models, J. Chem. Phys. 94 (1991) 5650–5654.

[36] G.D. Smith, D.Y. Yoon, Equilibrium and dynamic properties of polymethylene melts from molecular dynamics simulations I. *n*-Tridecane, J. Chem. Phys. 100 (1994) 649–658.

[37] M. Mondello, G.S. Grest, Molecular dynamics of linear and branched alkanes, J. Chem. Phys. 103 (1995) 7156–7165.

[38] S. Murad, The viscosity of dense fluid mixtures: Mixing rules reexamined using nonequilibrium molecular dynamics, AIChE J. 32 (1986) 513–516.

[39] S.H. Lee, P.T. Cummings, Shear viscosity of model mixtures by nonequilibrium molecular dynamics I. Argon–krypton mixtures, J. Chem. Phys. 99 (1993) 3919–3925.

[40] S.H. Lee, P.T. Cummings, Shear viscosity of model mixtures by nonequilibrium molecular dynamics II. Effect of dipolar interactions, J. Chem. Phys. 105 (1996) 2044–2055.

[41] D.M. Heyes, Molecular dynamics simulations of liquid binary mixtures: partial properties of mixing and transport coefficients, J. Chem. Phys. 96 (1992) 2217–2227.

[42] D.R. Wheeler, R.L. Rowley, Shear viscosity of polar liquid mixtures via non-equilibrium molecular dynamics: water, methanol and acetone, Mol. Phys. 94 (1998) 555–564.

[43] A. Kopf, B. Dünweg, W. Paul, Dynamics of polymer "isotope" mixtures: molecular dynamics simulation and Rouse model analysis, J. Chem. Phys. 107 (1997) 6945–6955.

[44] M.L. Gee, P.M. McGuiggan, J.N. Israelachvili, A.M. Homola, Liquid to solid like transitions of molecularly thin films under shear, J. Chem. Phys. 93 (1990) 1895–1906.

[45] U. Landman, W.D. Luedtke, J. Gao, Atomic-scale issues in tribology: interfacial junctions and nano-elasto hydrodynamics, Langmuir 12 (1996) 4514–4528.

[46] J.C. Dijt, M.A.C. Stuart, G.J. Fleer, Competitive adsorption kinetics of polymers differing in length only, Macromolecules 27 (1994) 3219–3228.

[47] T.K. Xia, U. Landman, Molecular dynamics of adsorption and segregation from an alkane mixture, Science 261 (1993) 1310–1312.

[48] U. Landman, W.D. Luedtke, J. Ouyang, T.K. Xia, Nanotribology and the stability of nanostructures, Jpn. J. Appl. Phys. 32 (1993) 1444–1462.

[49] A. Yethiraj, Monte-Carlo simulation of confined semiflexible polymer melts, J. Chem. Phys. 101 (1994) 2489–2497.

[50] H.W. Hu, G.A. Carson, S. Granick, Relaxation time of confined liquids under shear, Phys. Rev. Lett. 66 (1991) 2758–2761.

[51] P.A. Thompson, G.S. Grest, M.O. Robbins, Phase transitions and universal dynamics in confined films, Phys. Rev. Lett. 68 (1992) 3448–3451.

[52] M.P. Allen, D.J. Tildesley, Computer Simulation of Liquids, Clarendon Press, Oxford, 1987.

[53] D.J. Evans, G.P. Morris, Statistical Mechanics of Nonequilibrium Liquids, Academic Press, London, 1990.

[54] P.T. Cummings, D.J. Evans, Nonequilibrium molecular dynamics approaches to transport properties and non-Newtonian fluid rheology, Ind. Eng. Chem. Res. 31 (1992) 1237–1252.

[55] S. Nosé, Constant temperature molecular dynamics methods, Progr. Theor. Phys. Suppl. 103 (1991) 1–46.

[56] R.B. Bird, W.E. Stewart, E.N. Lightfoot, Transport Phenomena, Wiley, New York, 1960.

[57] W.G. Hoover, Non-equilibrium molecular dynamics, Ann. Rev. Phys. Chem 34 (1983) 103–127.

[58] A.W. Lees, S.F. Edwards, The computer study of transport processes under extreme conditions, J. Phys. C 5 (1972) 1921–1929.

[59] G.J. Martyna, M.L. Klein, M. Tuckerman, Nosé–Hoover chains: the canonical ensemble via continuous dynamics, J. Chem. Phys. 97 (1992) 2635–2643.

[60] M. Tuckerman, B.J. Berne, G.J. Martyna, Reversible multiple timescale molecular dynamics, J. Chem. Phys. 97 (1992) 1990–2001.

[61] J.I. Siepmann, M.G. Martin, C.J. Mundy, M.L. Klein, Intermolecular potentials for branched alkanes and the vapour-liquid phase equilibria of *n*-heptane, 2-methylhexane, and 3-ethylpentane, Mol. Phys. 90 (1997) 687–693.

[62] M.G. Martin, J.I. Siepmann, Transferable potentials for phase equilibria. 1. United-atom description of *n*-alkanes, J. Phys. Chem. B 102 (1998) 2569–2577.

[63] J.I. Siepmann, S. Karaborni, B. Smit, Simulating the critical behavior of complex fluids, Nature 365 (1993) 330–332.

[64] B. Smit, S. Karaborni, J.I. Siepmann, Computer simulations of vapor-liquid phase equilibria of *n*-alkanes, J. Chem. Phys. 102 (1995) 2126–2140.

[65] B. Smit, S. Karaborni, J.I. Siepmann, Erratum: computer simulations of vapor-liquid phase equilibria of *n*-alkanes [J. Chem. Phys. 102 (1995) 2126], J. Chem. Phys. 109(1995) (1998) 352.

[66] W.L. Jorgensen, J.D. Madura, C.J. Swenson, Optimized intermolecular potential functions for liquid hydrocarbons, J. Am. Chem. Soc. 106 (1984) 6638–6646.

[67] A. Aucejo, M.C. Burguet, R. Munoz, J.L. Marques, Densities, viscosities, and refractive indices of some *n*-alkane binary liquid systems at 298.15 K, J. Chem. Eng. Data 40 (1995) 141–147.

[68] E.L. Heric, J.G. Brewer, Viscosity of some binary liquid nonelectrolyte mixtures, J. Chem. Eng. Data 12 (1967) 574–583.

[69] H. Ertl, F.A.L. Dullen, Self-diffusion and viscosity of some liquids as a function of temperature, AIChE J. 19 (1973) 1215–1223.

[70] J.H. Dymond, K.R. Harris, The temperature and density dependence of the self-diffusion coefficient of *n*-hexadecane, Mol. Phys. 75 (1992) 461–466.

[71] R.L. Rowley, Statistical Mechanics for Thermophysical Property Calculations, PTR, Prentice-Hall, New York, Englewood Cliffs, NJ, 1994.

[72] J.M. Dealy, K.F. Wissbrun, Melt Rheology and its Role in Plastics Processing, Van Nostrand Reinhold, New York, 1990.

[73] W. Gleissle, Two simple time-shear rate relations combining viscosity and first normal stress coefficient in the linear and non-linear flow range, in: G. Astarita, G. Marucci, L. Nicolais (Eds.), Rheology (Proceedings of the Eighth International Congress on Rheology) vol. 2, Plenum Press, New York, 1980, p. 457.

[74] W.P. Cox, E.H. Merz, Correlation of dynamic and steady-state viscosities, J. Polym. Sci. 28 (1958) 619–622.

[75] R.B. Bird, R.C. Armstrong, O. Hassager, Dynamics of Polymeric Liquids, vol. 1, Fluid Mechanics, Wiley, New York, 1977.

[76] G.J. Martyna, M.E. Tuckerman, D.J. Tobias, M.L. Klein, Explicit reversible integrators for extended systems dynamics, Mol. Phys. 87 (1996) 1117–1157.